RSC Advances

PAPER

View Article Online
View Journal | View Issue

Cite this: *RSC Adv.*, 2024, **14**, 36181

Porous $CaMnO_3$-promoted g-C_3N_4 as an effective photocatalyst for tetracycline degradation†

Bo Zhang,[a] Chaoqi Li,[a] Shasha Liu,[a] Lixuan Zhuang,[a] Weiqi Zhang,[a] Limei Huang,[a] Zhenzhen Jia,[b] Dongdong Chen *[a] and Xiang Li*[a]

A $CaMnO_3$/g-C_3N_4 heterostructure, demonstrating promising photocatalytic performance for tetracycline (TC), was successfully synthesized using a straightforward calcination approach in this study. A series of characterization methods were employed to assess the physicochemical properties and visible-light responsiveness of the synthesized photocatalysts. The photocatalytic degradation rates of TC for the three prepared samples were evaluated. The results indicate that the $CaMnO_3$/g-C_3N_4 composite exhibits the highest photocatalytic activity under visible-light irradiation, surpassing that of the individual components. Specifically, the degradation rate of $CaMnO_3$/g-C_3N_4 is 0.031 min^{-1}, which is 2.07 and 2.82 times greater than that of the pristine g-C_3N_4 and $CaMnO_3$, respectively. Our findings highlight the significant potential of eco-friendly perovskites in developing visible-light-activated g-C_3N_4-based heterostructures for practical photocatalytic applications.

Received 5th September 2024
Accepted 5th November 2024

DOI: 10.1039/d4ra06407k

rsc.li/rsc-advances

1 Introduction

As urbanization progresses rapidly, environmental challenges and associated risks are on the rise, with water contamination by organic pollutants (*e.g.* TC) emerging as a particularly severe concern for human well-being.[1–4] Over the past few decades, semiconductor-based photocatalysis has proven to be one of the most effective technologies for removing TC from wastewater.[2,3,5–7] More recently, metal-free photocatalysts have garnered widespread attention due to their exceptional physicochemical properties and excellent stability.[4–8] Among these, graphitic carbon nitride (*i.e.* g-C_3N_4) stands out due to its numerous advantages, including the optimal band gap (*i.e.*, 2.7 eV), strong robustness, and cost-effectiveness. These merits have made g-C_3N_4 increasingly promising for visible-light induced photocatalysis in recent years.[6,8–12] However, the practical application of bare g-C_3N_4 is limited by its poor photocatalytic efficiency, stemming from inadequate visible-light absorption and extremely low charge carrier separation efficiency.[13–17] Consequently, various methods have been explored by researchers to address these limitations, such as morphology modification, element doping, and heterojunction construction.[14–16,18,19] Among these methods, heterojunction construction has been shown to be one of the most effective approaches. It not only facilitates the separation and transport of photogenerated charges but also enhances the visible light responsiveness of g-C_3N_4.[20–22]

Perovskite oxides with an ABO_3 structure are among the most promising heterogeneous catalysts for environmental remediation due to their tunable crystal structures, optical and chemical stability, adjustable band gaps, long charge carrier lifetimes, and sufficient oxygen vacancies.[23–26] Additionally, the transition metals within these perovskite oxides exhibit variable oxidation states, which facilitate electron movement, making them valuable as electron transport materials in the design of electrocatalysts and photocatalysts.[27,28] In the structure of perovskite oxides, the A sites are typically occupied by larger alkaline or rare earth metals (*e.g.*, Ca, La, Be, Ba), while the B sites are filled by transition metals (*e.g.*, Mn, Co, Sr, Ti, Ni), with A representing a divalent cation and B a tetravalent cation.[29,30] Among them, Mn-based perovskites are noted for their oxidative stability, temperature resistance, and good conductivity for both oxygen and electrons, making them widely used in catalytic reactions.[30] Calcium manganite (*i.e.* $CaMnO_3$) is a significant member of this group, characterized by a framework of MnO_6 octahedrons with Ca located in the interstitial spaces.[31–33] The raw materials for synthesizing $CaMnO_3$ are environmentally friendly, non-toxic, earth-abundant, and cost-effective, thus leading to increased demand for its application across various fields.[31–34] Furthermore, $CaMnO_3$ possesses an extremely narrow band gap, allowing it to effectively absorb visible light in the photocatalytic reactions.[34,35] Therefore, it is reasonable to propose that forming a heterojunction between g-C_3N_4 and narrow-gap $CaMnO_3$ could enhance both the separation efficiency of photogenerated electron–hole pairs and the

[a]*School of Environmental and Chemical Engineering, Guangdong Provincial Key Laboratory of Eco-environmental Studies and Low-carbon Agriculture in Peri-urban Areas, Zhaoqing University, 526061 Zhaoqing, China*

[b]*School of Environmental Science and Engineering, Sun Yat-Sen University, 510006 Guangzhou, China*

† Electronic supplementary information (ESI) available. See DOI: https://doi.org/10.1039/d4ra06407k

ability to harvest visible light. Notably, the hybridization of g-C_3N_4 with $CaMnO_3$ perovskite oxides has been relatively underexplored in existing literature, warranting further investigation.

In this study, a novel $CaMnO_3$/g-C_3N_4 heterojunction was created through a straightforward calcination process. The morphology and structure of the catalysts were characterized using field emission scanning electron microscopy (FE-SEM), transmission electron microscopy (TEM), and X-ray diffraction (XRD). Optical properties were assessed through UV-vis Diffuse reflectance spectroscopy (UV-vis DRS) and Fourier transform infrared spectroscopy (FT-IR), while X-ray photoelectron spectroscopy (XPS) was employed to determine the chemical composition of the samples. The separation efficiency of photogenerated charge carriers including electrons (e^-) and holes (h^+) was evaluated *via* the photoluminescence (PL) and Photoelectrochemical measurements. The photocatalytic performance of the as-prepared samples under the irradiation of visible light was investigated using TC as a model pollutant. The results demonstrated that the inclusion of $CaMnO_3$ significantly improved the photocatalytic activity of the $CaMnO_3$/g-C_3N_4 composite compared to the bare g-C_3N_4. The findings indicate that the notable photocatalytic performance of $CaMnO_3$/g-C_3N_4 is attributed to its effective visible-light harvesting ability and higher separation efficiency of photogenerated carriers. This study explores a new idea for the development of highly efficient and robust heterostructures for use in environmental remediation.

2 Materials and methods

2.1 Materials

Calcium nitrate tetrahydrate ($Ca(NO_3)_2 \cdot 4H_2O$, 99%), manganese nitrate solution ($Mn(NO_3)_2$, 50 wt% in H_2O), ammonium carbonate ($(NH_4)_2CO_3$), ammonium bicarbonate (NH_4HCO_3, ≥99.0%) and melamine ($C_3H_6N_6$) were purchased from Aladdin Ltd. The concentrated hydrochloric acid (HNO_3) was purchased from Guangzhou Chemical reagent Factory. In this research, all the chemicals were directly used without further purification.

2.2 Catalysts syntheses

2.2.1 Synthesis of porous $CaMnO_3$ microspheres. The synthesis of $CaMnO_3$ microspheres followed a previously reported method with some modifications.[36] Specifically, 0.1 mol $(NH_4)_2CO_3$ was dissolved in 100 mL of H_2O and equimolar NH_4HCO_3 was dissolved in another 100 mL of H_2O. Subsequently, $Mn(NO_3)_2$ (0.05 mol) and $Ca(NO_3)_2$ (0.05 mol) were separately added to the respective solutions. After stirring for 30 minutes, the above two solutions were filtered, resulting in the formation of dried $MnCO_3$ and $CaCO_3$ solids at 70 °C overnight. Then the two carbonate species (mole ratio of $MnCO_3/CaCO_3 = 1:1$) were then dissolved in dilute nitric acid, followed by the addition of a specific amount of $(NH_4)_2CO_3$ with $((Ca^{2+} + Mn^{2+}) : CO_3^{2-} = 1:2.5)$ under constant stirring for 30 min. After that, the solution was filtered, and the resulting precipitate was washed before dried overnight (70 °C). These processes ultimately resulted in the formation of $CaMn(CO_3)_2$ spheres. The final porous $CaMnO_3$ microspheres was synthesized by annealing $CaMn(CO_3)_2$ precursors at 900 °C for 5 h at a heating rate of 5 °C min^{-1}.

2.2.2 Synthesis of $CaMnO_3$/g-C_3N_4 heterostructures. The synthesis of $CaMnO_3$/g-C_3N_4 heterostructures involved a series of steps. Initially, the as-obtained $CaMnO_3$ and melamine ($C_3H_6N_6$) were mixed and subjected to thermal treatment at 550 °C for 4 hours at a heating rate of 5 °C min^{-1}. Specifically, $CaMnO_3$ powder (1 g) was combined with melamine (10 g) and thoroughly ground for 30 minutes to yield a resultant mixture. Subsequently, to obtain the final $CaMnO_3$/g-C_3N_4 product, the above mixture was transferred to a furnace and treated at 550 °C for 4 hours under atmospheric conditions with a heating rate of 5 °C min^{-1}. Additionally, pure g-C_3N_4 was synthesized using the same procedure, excluding the addition of $CaMnO_3$.

2.3 Catalyst characterization

The physicochemical properties of the obtained samples were comprehensively characterized using various techniques, including N_2 physisorption, XRD, UV-vis DRS, FT-IR, FE-SEM, TEM, XPS, and PL analysis. N_2 physisorption tests were utilized to determine the specific surface area of the catalysts, with measurements performed using the Brunauer–Emmett–Teller (BET) method on an ASAP 2020 system at 77 K. XRD patterns were acquired using a Bruker D8-Advance diffractometer with Cu Kα radiation. UV-vis DRS spectra, covering the range of 250–800 nm, were recorded with a UV-vis spectrophotometer (UV-2600, Shimadzu, Japan), employing $BaSO_4$ as the reflectance standard. FT-IR spectra were obtained using a FT-IR spectrometer (FTIR-8400S, Shimadzu, Japan). The morphologies of the photocatalysts were examined using FE-SEM and TEM, conducted on a ZEISS ULTRA 55 scanning electron microscope and an FEI Talos F200X transmission electron microscope, respectively. XPS spectra were recorded on a Thermo Fisher ESCALAB 250 system, utilizing monochromatic Al Kα (1486.8 eV) radiation as the X-ray source. PL measurements were performed at ambient temperature using a HITACHI F-7000 PL spectrophotometer. Additionally, electron spin resonance (ESR) measurements under visible light irradiation were conducted on a Bruker spectrometer (JES-FA300) to investigate the active radicals, employing 5,5-dimethyl-L-pyrroline *N*-oxide (DMPO) as the spin-trapping reagent.

2.4 Photoelectrochemical measurements

Photoelectrochemical measurements were conducted using a CHI 660D workstation, with a 0.5 M Na_2SO_4 aqueous solution serving as the electrolyte. Photocurrent response tests were performed in this electrolyte under illumination from a 300 W Xe lamp. Electrochemical impedance spectroscopy (EIS) measurements were carried out in Na_2SO_4 solution at an AC voltage of 10 mV over a frequency between 10^5 and 10^{-1} Hz. The working electrode was prepared through the following steps: First, 30 mg of the obtained sample was combined with 1 mL of ethylene glycol, 1 mL of ethanol, and 20 μL of a 0.5% Nafion solution to create a slurry under ultrasonic conditions. Next,

approximately 50 μL of the prepared slurry was uniformly coated onto a 1 cm × 1 cm FTO glass substrate. Finally, the coated FTO glass was dried in a vacuum oven at 60 °C for 8 hours.

2.5 Photocatalytic tests

The photocatalytic performances of the catalysts were assessed in a photoreactor using a 300 W xenon lamp equipped with a 420 nm filter to simulate visible light. In each test, 50 mg of photocatalyst was introduced into a 50 mL solution of TC (10 mg L^{-1}) and stirred for half an hour in the absence of light. Following the dark reaction, 3 mL of the suspension was periodically withdrawn at specified time intervals (*e.g.*, 15 minutes) and filtered using 0.45 μm filter membranes for analysis on a UV-vis spectrophotometer at the maximum absorption wavelength of TC (357 nm). The entire reaction under visible-light irradiation lasted for 90 minutes. The reaction kinetics of the photocatalysts for TC degradation followed the pseudo-first order reaction kinetics model: $\ln(C_0/C_t) = kt$, where C_0 and C_t represent the initial and current reactant concentrations of TC solution, respectively, and k denotes the pseudo-first-order rate constant.

3 Results and discussions

The XRD patterns in Fig. 1 reveal the phase and crystal characteristics of the as-prepared samples. Specifically, the multi diffraction peaks at $2\theta = 23.9°$, 33.9°, 48.8° and 60.7° presented in Fig. 1 could be attributed to (101), (121), (202) and (321) crystalline planes of $CaMnO_3$ material (JCPDS file no.76-1132).[36] Additionally, the distinctive diffraction peaks at $2\theta = 13.2°$ and 27.6° correspond to the (100) and (002) lattice planes of g-C_3N_4, representing the in-plane repeated tri-*s*-triazine units and the stacked conjugated aromatic system, respectively.[7,10,18] The detectable presence of characteristic diffraction peaks from both $CaMnO_3$ and g-C_3N_4 phases in the $CaMnO_3$/g-C_3N_4 composite suggests the successful combination of $CaMnO_3$ with the g-C_3N_4 sample.

The FT-IR method was employed to further elucidate the chemistry states on the surface of $CaMnO_3$, g-C_3N_4 and $CaMnO_3$/g-C_3N_4 samples, as depicted in Fig. 2. In the FT-IR spectrum of g-C_3N_4, the prominent peak at 811 cm^{-1} is attributed to the characteristic breathing modes of the triazine units, while the absorption bands ranging from 1000 to 1700 cm^{-1} are assigned to the typical stretching vibration modes of C–N and C=N (*i.e.*, N–C=N heterocycles) within the "melon" framework.[7,10,18,23] Meanwhile, the FT-IR spectrum of $CaMnO_3$ displays wide bands between 560 and 580 cm^{-1}, corresponding to the stretching vibration of the Mn–O or Mn–O–Mn bonds, which is indicative of the typical perovskite structure formation.[37,38] Additionally, the absorption band at 435 cm^{-1} is attributed to the bending mode resulting from changes in the Mn–O–Mn bond angle.[37,38] The FT-IR spectra of the $CaMnO_3$/g-C_3N_4 composite reveal the presence of all characteristic peaks of g-C_3N_4 and $CaMnO_3$, indicating the successful construction of the heterostructure.

The light absorption capability is a crucial property that significantly influences the photocatalytic performance of semiconductors. To evaluate this, the light absorption properties of the synthesized samples were examined using UV-vis DRS measurements, with the results presented in Fig. 3. As shown in Fig. 3a, the light absorption edge of the pristine g-C_3N_4 is approximately 455 nm, indicating strong absorption in the UV region.[6,9] In contrast, the bare $CaMnO_3$ exhibits light absorption across both the UV and visible regions, demonstrating its efficient photoelectrical properties, similar to those observed in $LaCoO_3$ perovskite oxide.[39] When g-C_3N_4 is combined with $CaMnO_3$, the light absorption edge experiences a red shift,

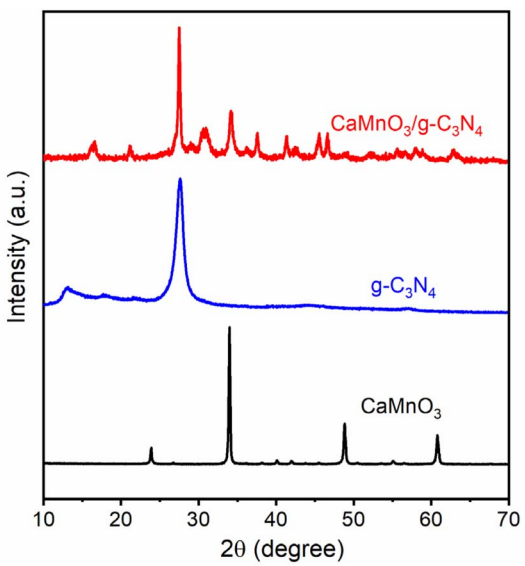

Fig. 1 XRD patterns of as-obtained photocatalysts of g-C_3N_4, $CaMnO_3$ and $CaMnO_3$/g-C_3N_4 composite.

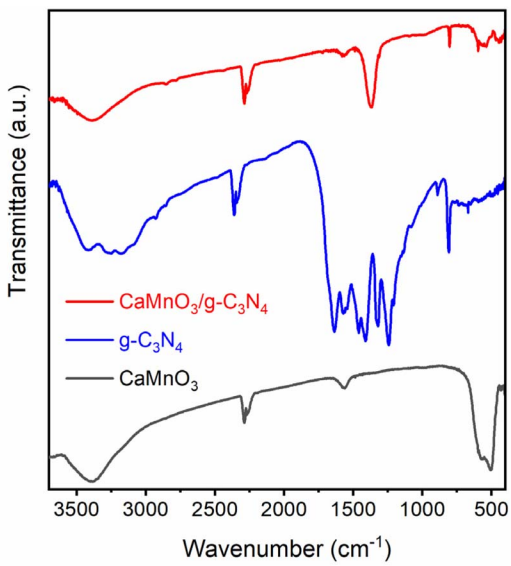

Fig. 2 FT-IR spectra of as-obtained g-C_3N_4, $CaMnO_3$ and $CaMnO_3$/g-C_3N_4 composites.

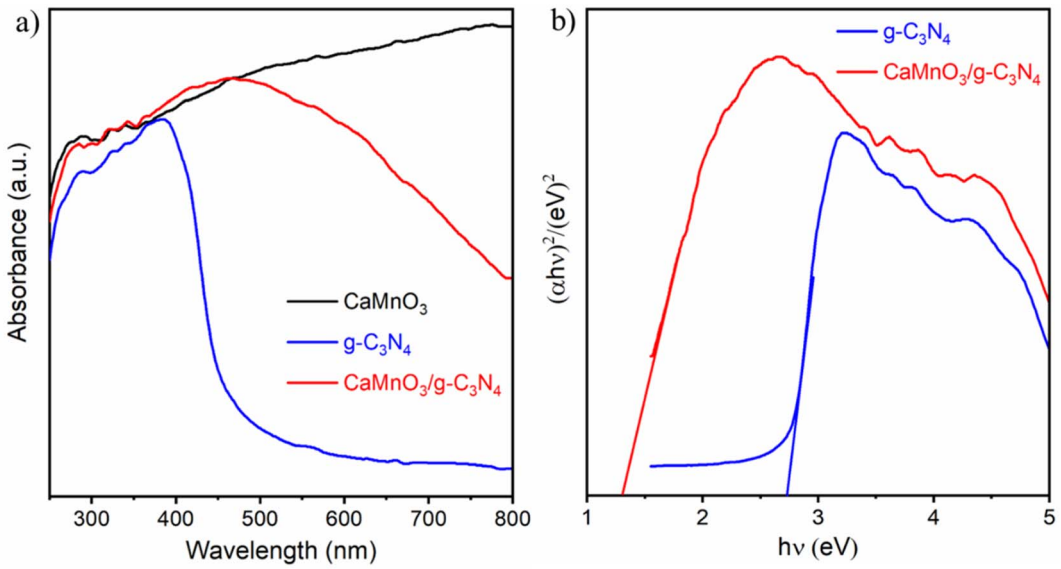

Fig. 3 (a) UV-vis diffuse reflectance spectra of g-C_3N_4, $CaMnO_3$ and $CaMnO_3$/g-C_3N_4 samples; (b) $(\alpha h\nu)^2 - h\nu$ plots of g-C_3N_4 and $CaMnO_3$/g-C_3N_4 samples determined by Kubelka–Munk formula.

which corresponds to an enhanced ability to absorb visible light. The bandgap energies of the photocatalysts were calculated using the Kubelka–Munk formula:

$$\alpha(h\nu) = A(h\nu - E_g)^{n/2}$$

wherein α is the absorption coefficient, A is a proportionality constant, and E_g is the band gap energy. Here, $h\nu$ represents photon energy, with h being the Planck constant and ν the light frequency. The value of n is determined by the type of electronic transition in the specific semiconductor. As illustrated in Fig. 3b, the band gaps of g-C_3N_4 and $CaMnO_3$/g-C_3N_4 are calculated to be 2.73 and 1.3 eV, respectively. From Fig. 3, it is evident that the $CaMnO_3$/g-C_3N_4 composite exhibits enhanced visible light harvesting capability compared to the bare g-C_3N_4, which can be attributed to the strong visible light response of the $CaMnO_3$ perovskite. This finding indicates the successful formation of the $CaMnO_3$/g-C_3N_4 heterostructure.

The BET specific surface area and pore size distributions of the materials were analyzed using N_2 adsorption–desorption isotherms, as depicted in Fig. 4. It is evident that all the samples exhibit type IV isotherms with type H3 hysteresis loops (Fig. 4a), indicating the presence of a mesoporous structure. Specifically, the BET specific surface areas of $CaMnO_3$, g-C_3N_4, and $CaMnO_3$/g-C_3N_4 are calculated to be 4.07, 23.07, and 25.72 $m^2\ g^{-1}$, respectively. Following the introduction of $CaMnO_3$, the BET specific surface area of $CaMnO_3$/g-C_3N_4 shows a slight improvement compared to the bare g-C_3N_4, while the pore volume decreases from 0.134 to 0.105 $cm^3\ g^{-1}$ (Table S1†). Fig. 3b presents the pore size distributions of the prepared samples calculated based on the Barrett–Joyner–Halenda (BJH) method, with the average pore sizes of $CaMnO_3$, g-C_3N_4, and $CaMnO_3$/g-C_3N_4 determined to be 8.06, 23.19, and 16.29 nm, respectively. Consequently, the reduced pore volume in $CaMnO_3$/g-C_3N_4 is attributed to the formation of a greater number of smaller-sized pores during the calcination process of the composite. These results indicate that the introduction of $CaMnO_3$ perovskite oxide into the g-C_3N_4 system provides the composite with more reactive sites and an enhanced ability to absorb smaller molecules, which is favorable for photocatalytic reactions.

The surface morphologies of the as-prepared catalysts were analyzed using SEM and TEM measurements, with the results presented in Fig. 5, 6, S1 and S2.† The representative SEM images in Fig. 5a and b reveal that the bare g-C_3N_4 displays a compact block structure assembled by irregular lamellar architectures. Meanwhile, the pure $CaMnO_3$ perovskite oxide exhibits a porous microspherical structure composed of aggregated nanoparticles (Fig. 5c and S1†). The SEM image of $CaMnO_3$/g-C_3N_4 composite (Fig. 5d and S2†) illustrates the interweaving of lamellar architectures with porous microspheres when $CaMnO_3$ perovskite oxide is mixed with g-C_3N_4. And it can be clearly seen that a significant quantity of small pores is formed in the structure of $CaMnO_3$/g-C_3N_4 as compared to the pristine g-C_3N_4, this finding is consistent with the outcomes obtained from N_2 adsorption–desorption measurements. Additionally, the close contact between $CaMnO_3$ and g-C_3N_4 is observed, which can facilitate the mass transfer and charge transport processes of the $CaMnO_3$/g-C_3N_4 composite in the photocatalytic reactions. Further investigation of the specific micro-structure of the $CaMnO_3$/g-C_3N_4 composite was conducted using TEM method, as indicated in Fig. 6. The images at three different magnifications (Fig. 6a–c) reveal that a large amount of $CaMnO_3$ nanoparticles is deposited on the surface of g-C_3N_4 nanosheets, indicating successful hybridization of $CaMnO_3$ with g-C_3N_4. Fig. 6d presents the high-resolution TEM (*i.e.* HRTEM) image of the $CaMnO_3$/g-C_3N_4 catalyst, showing a fringe spacing of 0.26 nm corresponding to

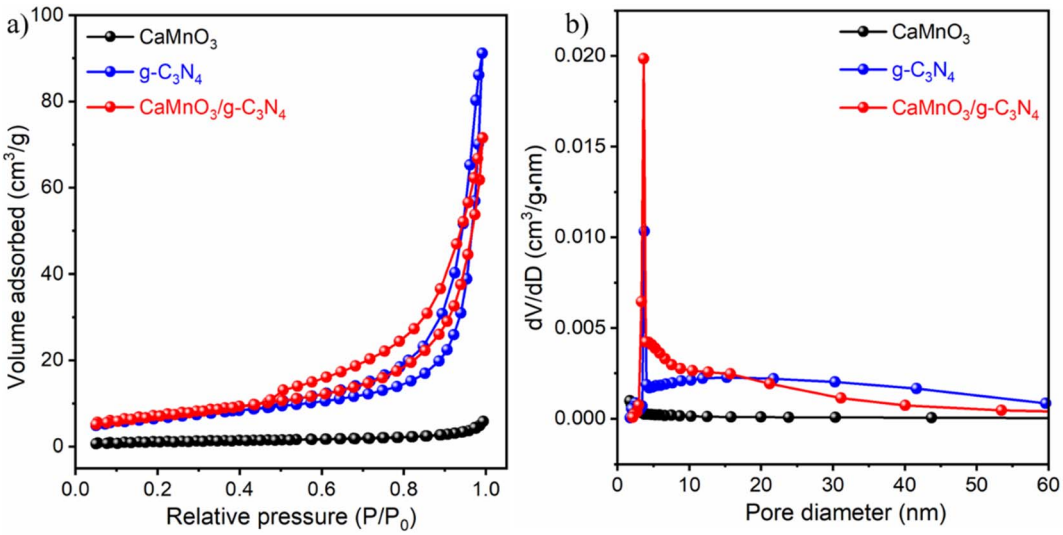

Fig. 4 (a) N_2-adsorption and desorption isotherms and (b) Barrett–Joyner–Halenda (BJH) pore size distribution curves of g-C_3N_4, $CaMnO_3$ and $CaMnO_3$/g-C_3N_4 samples.

the typical inter-planar spacing of the (121) plane of $CaMnO_3$ perovskite material,[36] while the related lattice spacing of g-C_3N_4 is lost due to its extremely low crystallinity. In summary, the results of SEM and TEM further confirm the successful construction of a binary heterojunction between $CaMnO_3$ and g-C_3N_4, which aligns with the results of XRD and FT-IR measurements.

The XPS technology was utilized to analyze the chemical compositions and binding states of the as-obtained samples, as depicted in Fig. 7. The survey spectrum in Fig. 7a reveals the presence of C, O, N, Ca, and Mn elements in $CaMnO_3$/g-C_3N_4,

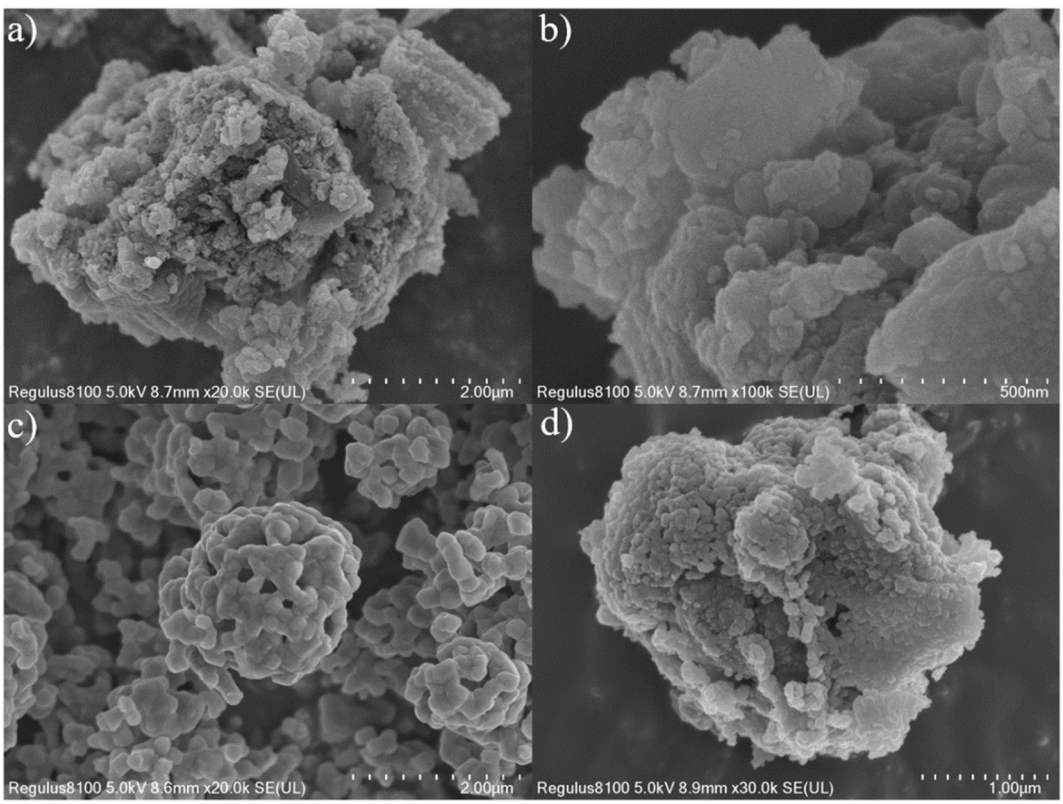

Fig. 5 The representative SEM image of pristine g-C_3N_4 (a and b), (c) $CaMnO_3$ and (d) $CaMnO_3$/g-C_3N_4 composite.

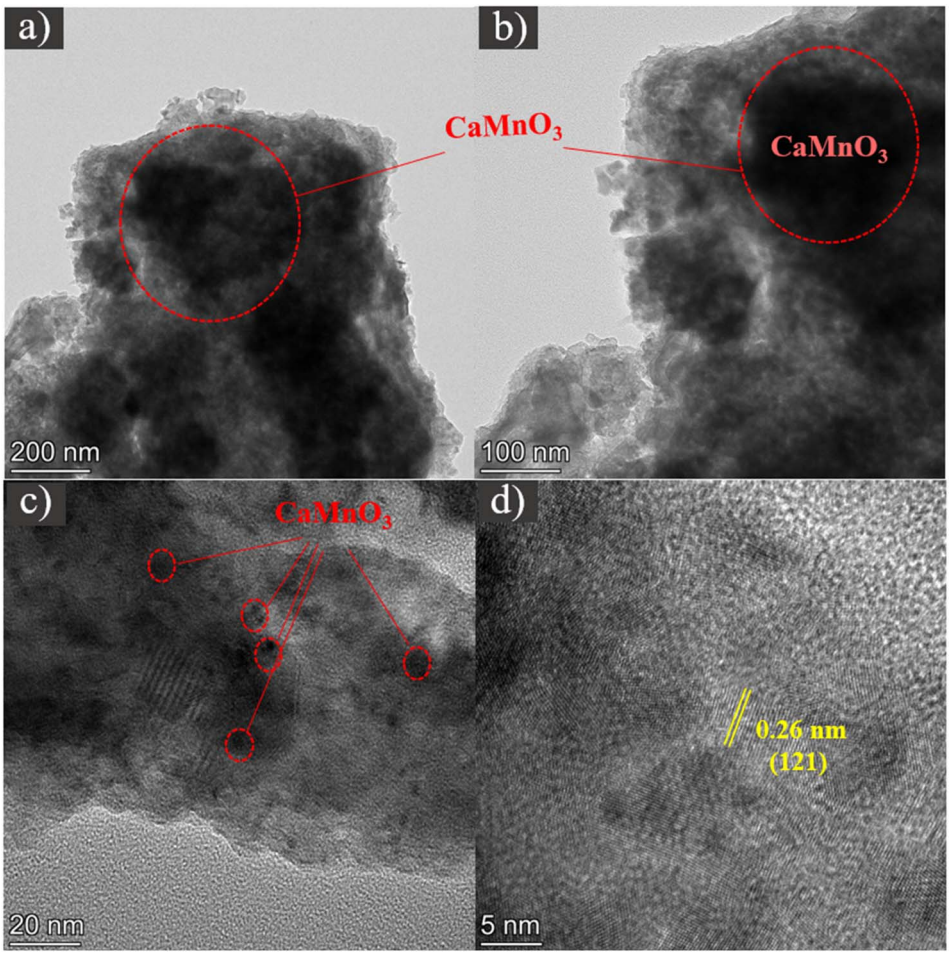

Fig. 6 TEM images (a–c) and HR-TEM images (d) of $CaMnO_3$/g-C_3N_4 photocatalysts.

whereas the other two catalysts ($CaMnO_3$ and g-C_3N_4) only contain a subset of these elements (Fig. S3†), indicating the successful synthesis of the binary composites. In the high-resolution XP C 1s spectrum (Fig. 7b), three representative peaks at 289.5, 285.9 and 284.8 eV corresponding to sp^2-bonded carbon (N–C=N), C–N bond, and sp^2 carbon (C=C or C–C bond) are observed.[40,41] The deconvoluted XP N 1s spectrum (Fig. 7c) reveals four distinct characteristic peaks at 403.8, 400.3, 399.1 and 398.3 eV corresponding to graphitic N, surface uncondensed amino groups bonded with an H atom (C–N–H), tertiary nitrogen bond (N–$(C)_3$), and sp^2 hybridized N (C=N–C).[40,42] Additionally, the XP O 1s spectrum (Fig. 7d) enables the differentiation of absorbed oxygen-containing species at approximately 532.1, 531.2, and 529.8 eV, respectively.[43,44] The former is corresponding to C=O, the middle is ascribed to the adsorbed oxygen species, and the latter arises from the metal oxygen bond (*i.e.* M–O).[41,44] The curve-fitting of XP Ca 2p spectrum (Fig. 7e) displays two peaks (with an energy gap of 3.5 eV) corresponding to Ca $2p_{1/2}$ and Ca $2p_{3/2}$ orbitals centered at 350.7 and 347.2 eV, indicating that that Ca in the composite is the divalent oxide form.[29,30] Fig. 7f exhibits the XP Mn 2p spectrum, and the binding energy gap between Mn $2p_{1/2}$ (653.5 eV) and Mn $2p_{3/2}$ (641.9 eV) spin–orbit splitting is about 11.6 eV, which is consistent with the previous works.[30,45] The doublet peaks can be further deconvoluted by six peaks centered at 656.5, 653.9, 652.9, 644.9, 642.3 and 641.3 eV, respectively. The main peaks located at 653.9 and 642.3 eV are attributed to Mn^{4+} ions, while the two peaks located at 652.9 and 641.3 eV are assigned to Mn^{3+} ions.[29,30] The other two bands at 656.5 and 644.9 eV are corresponding to the satellite peaks.[29,30] The results indicate that Mn^{4+} is dominant on the surface of $CaMnO_3$. The XPS measurements also demonstrate the successful preparation of $CaMnO_3$/g-C_3N_4.

The photocatalytic performance of a semiconductor is closely tied to the quantity of photo-generated charge carriers (e^- and h^+).[7,46] To assess the separation efficiency and the transport ability of photogenerated e^- and h^+, PL measurements, transient photocurrent response measurements and EIS tests were conducted, with the results presented in Fig. 8. Fig. 8a illustrates that the PL intensity of $CaMnO_3$/g-C_3N_4 sample significantly decreases compared to the pristine g-C_3N_4, indicating a substantial suppression of the recombination process of the charge carriers after $CaMnO_3$ loading. Moreover, no obvious emission peak is observed for the bare $CaMnO_3$, possibly due to its extremely narrow band gap.[47,48] The transient photocurrent spectra in Fig. 8b demonstrate that the $CaMnO_3$/

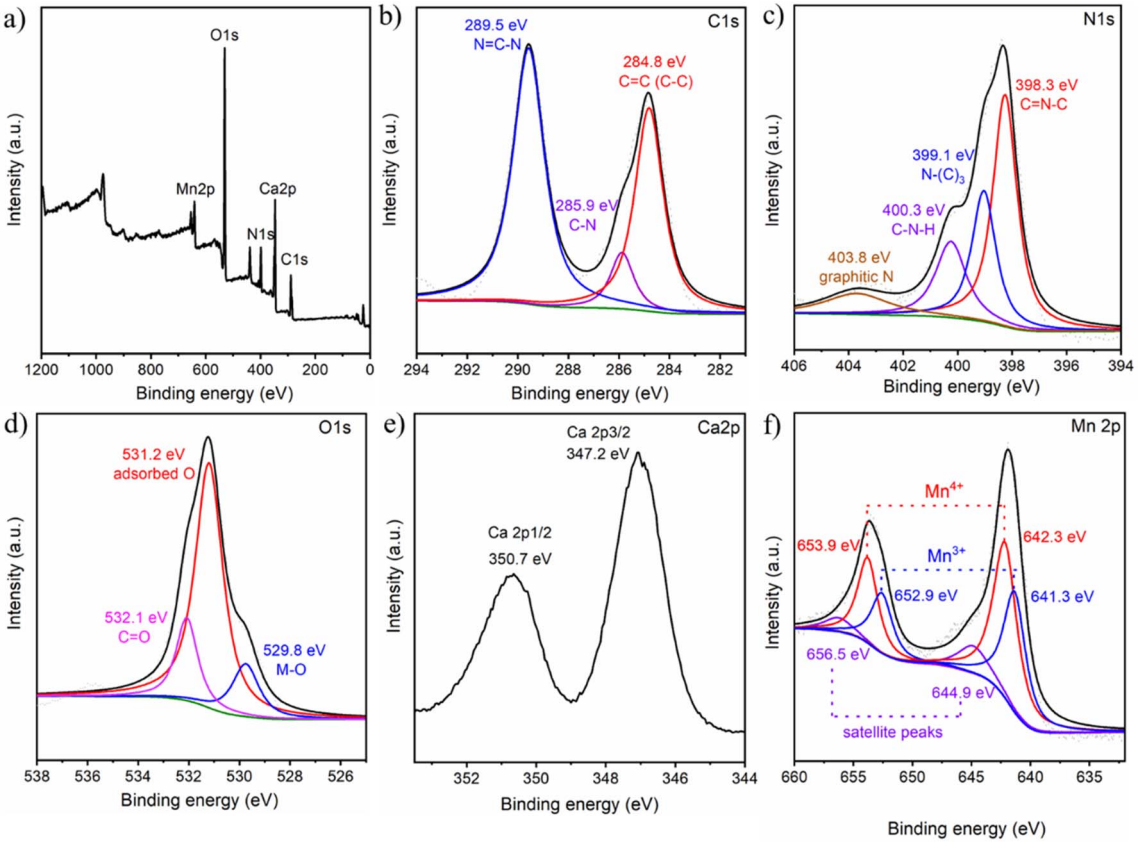

Fig. 7 The XPS survey spectra (a), high-resolution XP C 1s (b), N 1s (c), O 1s (d), Ca 2p (e) and Mn 2p (f) spectra for $CaMnO_3$/g-C_3N_4 photocatalysts.

g-C_3N_4 composite exhibits the highest photocurrent intensity compared to the pristine g-C_3N_4 and $CaMnO_3$. These results suggest that the introduction of $CaMnO_3$ enhances the separation efficiency of photogenerated electrons and holes. In summary, the PL and transient photocurrent analyses indicate that the hybridization of $CaMnO_3$ and g-C_3N_4 significantly promotes the interfacial transfer process of the photogenerated charge carriers. Moreover, EIS measurements were also conducted to study the interfacial charge transfer processes, with the results shown in Fig. 8c. The equivalent circuit used in the measurements is exhibited in the inset of Fig. 8c, it contains the solution resistance (*i.e.* R_s), the electron-transfer resistance (*i.e.* R_{ct}) as well as the constant phase element (CPE). R_s means the total resistance from the wire, electrolyte and electrode. R_s is mainly decided by the semiconductors due to fact that the measurement system is nearly identical except the electrode material.[44,49] R_{ct} is associated with the interfacial charge transfer between the electrode and electrolyte. Generally, a lower R_{ct}

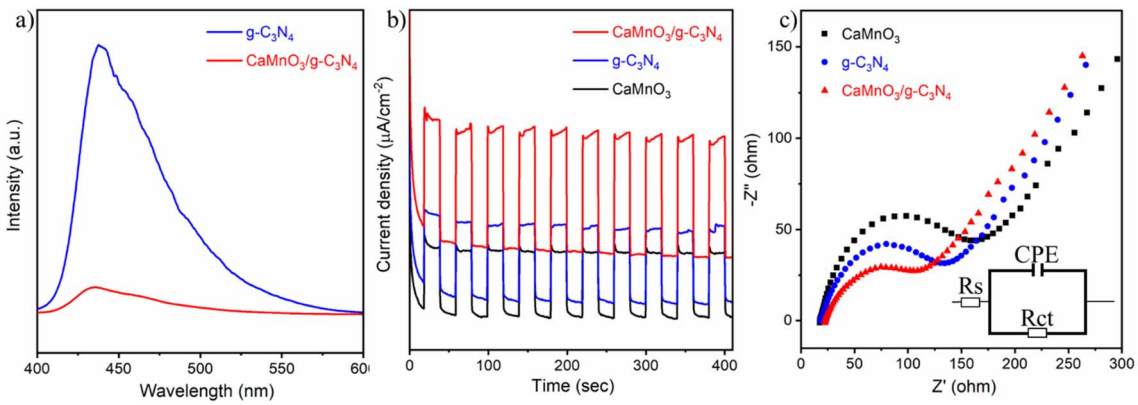

Fig. 8 (a) PL spectra, (b) transient photocurrent responses and (c) EIS Nyquist plots of the as-prepared photocatalysts.

value corresponds to a faster interfacial charge transfer process.[44,49] In other words, a smaller semicircle radius in the Nyquist plots suggests a lower charge transfer resistance across the electrolyte/electrode interface, corresponding to the higher separation efficiency of charge carriers.[44,49] It can be seen that $CaMnO_3$/g-C_3N_4 demonstrates the smallest arc radius in the three samples, suggesting that the composite possesses the highest separation efficiency of charge carriers. Based on the results of PL and photoelectrochemical measurements, it can be concluded that the recombination of the charge carriers is effectively inhibited because of the strong interaction between $CaMnO_3$ and g-C_3N_4.

To evaluate the photocatalytic performances of the catalysts, TC, a widely prevalent antibiotic in wastewater, was selected as the model pollutant.[50,51] The photocatalytic degradation activities of TC over the obtained catalysts were specifically tested under visible light irradiation, as depicted in Fig. 9. Each experiment involved a dark reaction period of approximately 30 minutes before light irradiation to establish a balance of TC adsorption and desorption processes over the photocatalysts. The results in Fig. 9a reveal that the photocatalytic performances of the three catalysts for TC degradation under visible-light irradiation follow the order: $CaMnO_3$/g-C_3N_4 > g-C_3N_4 > $CaMnO_3$, consistent with the photoelectrochemical measurements. Additionally, a blank experiment (without photocatalyst) was also conducted, the results indicate that TC cannot be degraded in the absence of photocatalysts (Fig. S4†). Clearly, among the catalysts, the $CaMnO_3$/g-C_3N_4 catalyst demonstrates the highest photocatalytic activity under visible light irradiation, achieving approximately 95% within 90 minutes, while $CaMnO_3$ and g-C_3N_4 achieve 66% and 74%, respectively. The performance of $CaMnO_3$/g-C_3N_4 sample in this work in comparison with the systems reported in the previous publications is provided in Table S2.† The $CaMnO_3$/g-C_3N_4 sample exhibits outstanding photocatalytic activity as compared to the reported samples in terms of catalyst dosage, pollutant concentration and degradation efficiency. Furthermore, the reaction kinetics in the TC degradation processes were analyzed by fitting all the degradation rates based on the typical pseudo-first-order correlation: $\ln(C_0/C) = kt$, where C_0 and C represent the initial TC concentration and the real-time TC concentration, k is the apparent pseudo-first-order rate constant (min^{-1}), and t indicates the reaction time. As shown in Fig. 9b, the apparent rate constants of $CaMnO_3$/g-C_3N_4, g-C_3N_4, and $CaMnO_3$ are calculated based on the above pseudo-first-order correlation, yielding values of 0.031, 0.015, and 0.011 min^{-1}, respectively. Obviously, among these, $CaMnO_3$/g-C_3N_4 exhibits the highest reaction rate constant, surpassing that of g-C_3N_4 and $CaMnO_3$ by 2.07 and 2.82 times, respectively.

In addition to its impressive performance, the stability and reusability of the photocatalyst is vital considerations for the practical applications. Consequently, the typical cycling experiments were performed under visible light irradiation to assess the stability of the $CaMnO_3$/g-C_3N_4 catalyst, with the results showcased in Fig. 10a. Clearly, only a marginal decrease (approximately 3%) in performance of degrading TC was observed for the $CaMnO_3$/g-C_3N_4 photocatalyst after 5 cycling tests. This slight reduction could be attributed to the inevitable loss of the photocatalyst during the cycling processes. The outcomes of the cycling experiments indicate that the $CaMnO_3$/g-C_3N_4 photocatalyst exhibits excellent stability and can be effectively reused for the photocatalytic degradation of TC in wastewater under visible light irradiation. In addition, XRD tests were further conducted to investigate the crystal structure of $CaMnO_3$/g-C_3N_4 before and after photocatalytic reaction, the results are shown in Fig. 10b. It indicates that the composite remains stable after the photo-degradation reaction, further indicating that $CaMnO_3$/g-C_3N_4 exhibits the commendable stability.

To uncover the reaction mechanism, the primary active species involved in the photocatalytic degradation process of TC over $CaMnO_3$/g-C_3N_4 were identified. It is well-established that $^{\bullet}OH$ and $^{\bullet}O^{2-}$ radicals, along with the photogenerated h^+, are key reactive species in the degradation reactions.[7,52] In order to

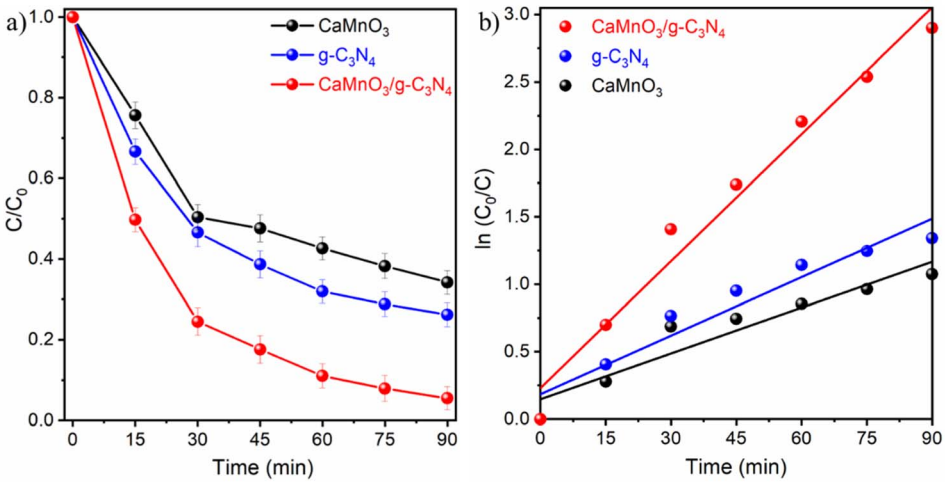

Fig. 9 (a) Photocatalytic performances and (b) pseudo-first-order kinetic plots of the as-obtained catalysts for degradation of TC under the irradiation of visible light.

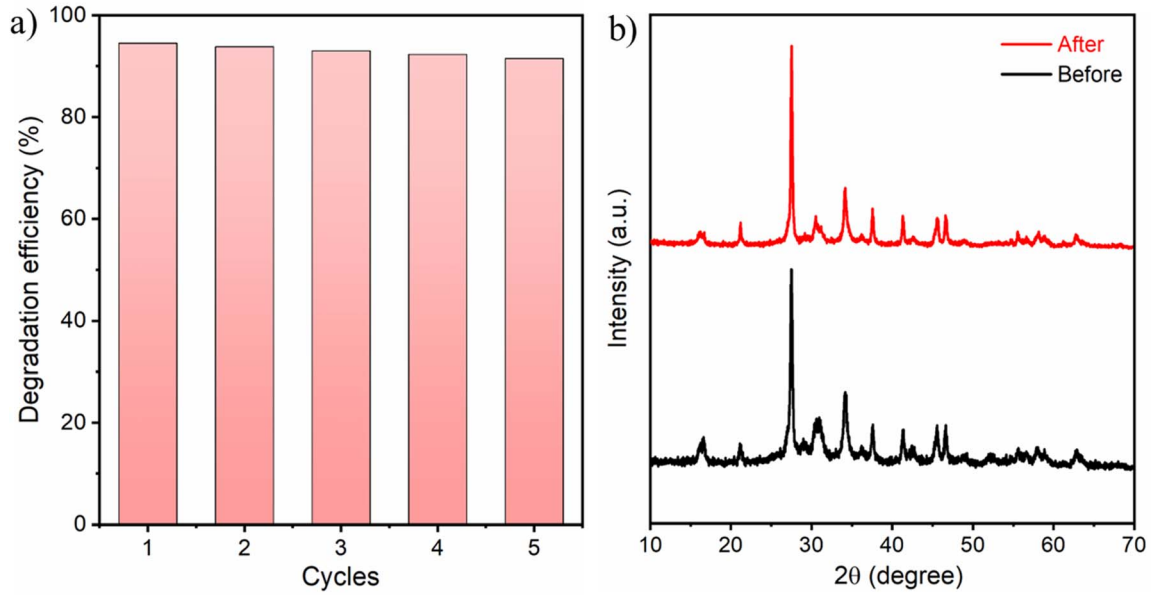

Fig. 10 (a) Cycling tests of $CaMnO_3$/g-C_3N_4 sample for the photocatalytic degradation of TC; (b) XRD spectra of $CaMnO_3$/g-C_3N_4 before and after the photocatalytic reaction.

investigate the role of the radicals in the photocatalytic degradation process of TC, the radical scavenging experiments were conducted. Herein, benzoquinone (*i.e.* BQ), *tert*-butyl alcohol (*i.e.* TBA) and ammonium oxalate (*i.e.* $(NH_4)_2C_2O_4$) are applied as the scavenging reagents of $^{\bullet}O_2^-$, $^{\bullet}OH$ and h^+, respectively.[7] The results, presented in Fig. 11, reveal that the photocatalytic performances for TC degradation using the $CaMnO_3$/g-C_3N_4 sample significantly decreases upon the addition of $(NH_4)_2C_2O_4$ scavengers, while TBA and BQ have minimal impact on the catalyst's activity, indicating that h^+ radicals are the primary active species. Specifically, the photocatalytic efficiency for TC degradation over $CaMnO_3$/g-C_3N_4 decreases to 28.9%, 62.4% and 78.6% after the addition of $(NH_4)_2C_2O_4$, BQ and TBA, respectively. Additionally, ESR tests were conducted to further explore the roles of free radicals in the reactions. In the ESR tests, DMPO was employed as a spin-trapping reagent, with results depicted in Fig. 12a and b. The ESR signals, with intensity ratios of 1 : 2 : 2 : 1 and 1 : 1 : 1 : 1, correspond to the DMPO-$^{\bullet}OH$ and DMPO-$^{\bullet}O^{2-}$ adducts, respectively, indicating the presence of both $^{\bullet}O^{2-}$ and $^{\bullet}OH$ radical species in the photocatalytic process. These findings align well with the radical trapping test results. Overall, the importance of radical species in the photocatalytic degradation of TC using $CaMnO_3$/g-C_3N_4 follows the order: $h^+ > {}^{\bullet}O^{2-} > {}^{\bullet}OH$.

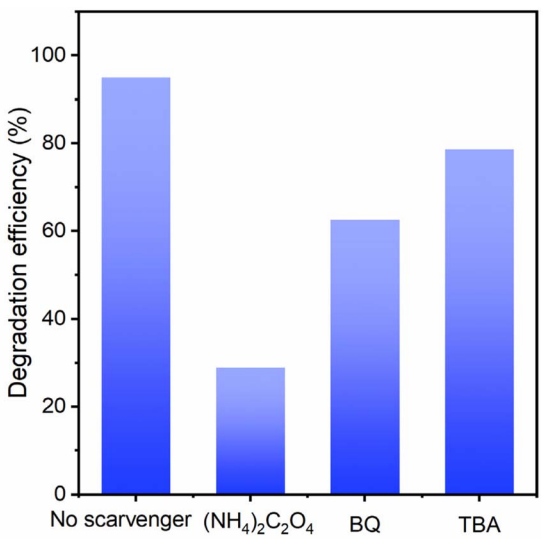

Fig. 11 Photocatalytic performance of $CaMnO_3$/g-C_3N_4 for TC degradation with different radical scavengers.

Based on the aforementioned observations, the potential degradation mechanism for TC is proposed, as depicted in Fig. 13. The increased surface area (25.72 $m^2\ g^{-1}$) of $CaMnO_3$/g-C_3N_4, along with its pore structures as indicated in Table S1,† facilitate TC adsorption process. Furthermore, the introduction of $CaMnO_3$ enhances the ability of g-C_3N_4 to capture more visible light. Under visible-light irradiation, g-C_3N_4 is excited to generate electrons (e^-) on the conduction band (CB) and h^+ on the valence band (VB). Due to the excellent conductivity of $CaMnO_3$, the e^- on the CB of g-C_3N_4 could easily transfer to $CaMnO_3$, thereby preventing the recombination process of e^- and h^+ in g-C_3N_4. According to the VB-XPS results (Fig. S5†), the VB value of $CaMnO_3$/g-C_3N_4 composite (1.51 eV) is slightly smaller than that of g-C_3N_4 (1.66 eV). Integrating the results presented in Fig. 3, the calculated CB potentials can be determined to be 0.21 eV and −1.07 eV, respectively. Evidently, the CB potential of $CaMnO_3$/g-C_3N_4 is not negative enough to reduce O_2 in water to produce $^{\bullet}O^{2-}$ ($O_2/{}^{\bullet}O^{2-} = -0.33$ eV), and the composite also cannot produce $^{\bullet}OH$ ($^{\bullet}OH/OH^- = 1.99$ eV).[53,54] Thus, h^+ in the composite should be responsible for the degradation of TC. Meanwhile, e^- remaining on the CB of g-

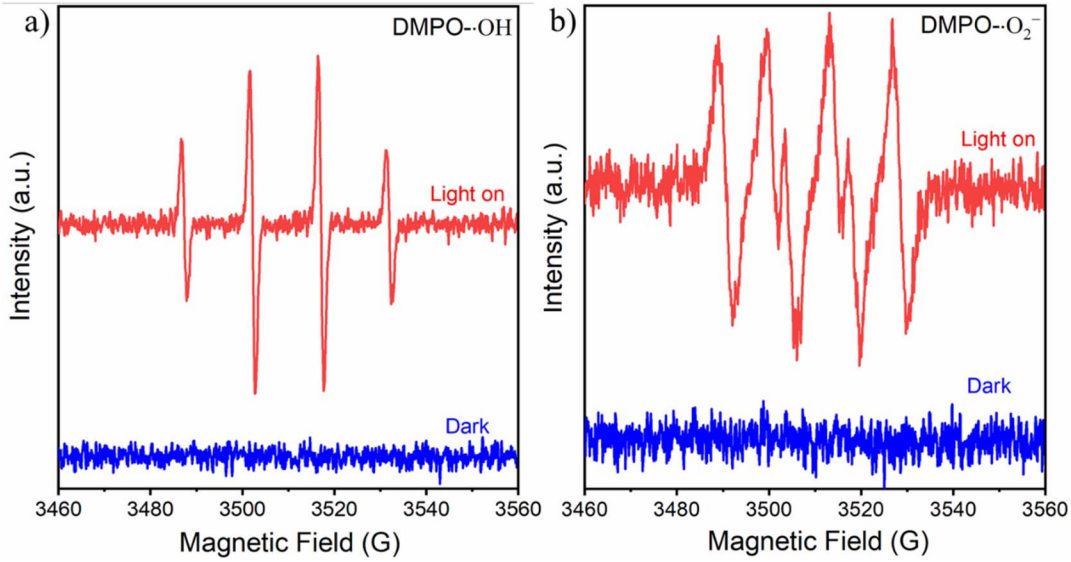

Fig. 12 ESR spectra of DMPO-$^{\cdot}O^{2-}$ (a) and DMPO-$^{\cdot}$OH (b) over the $CaMnO_3$/g-C_3N_4 composite.

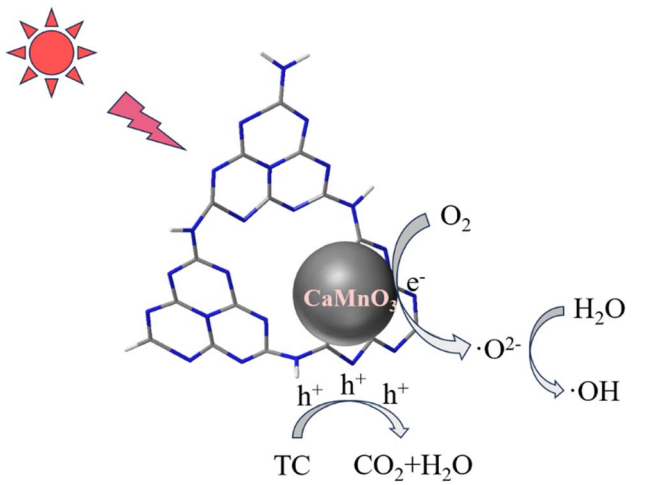

Fig. 13 Possible photocatalytic mechanism for TC degradation of $CaMnO_3$/g-C_3N_4.

C_3N_4 (−1.07 eV) can react with O_2 to produce $^{\cdot}O^{2-}$, and a portion of $^{\cdot}O^{2-}$ can further react with H_2O to produce $^{\cdot}$OH. In a whole, both h^+, $^{\cdot}$OH and $^{\cdot}O^{2-}$ participate in the degradation process of TC. However, h^+ plays the major role in degrading TC into smaller harmless molecules, such as CO_2 and H_2O.

4 Environmental implications

TC, a common antibiotic, poses significant challenges to human health and ecosystem security. Unfortunately, the practical application of photocatalysts for TC elimination was restricted by the insufficient charge transfer ability. In the present work, a novel efficient photocatalytic system (*i.e.* $CaMnO_3$/g-C_3N_4) was established and applied for TC degradation. Furthermore, the main active species participating in the photocatalytic reaction were identified and a potential photocatalytic degradation mechanism was proposed in this $CaMnO_3$/g-C_3N_4 system. This work demonstrates the effectiveness of using non-expensive photocatalysts in the actual wastewater treatment. Due to the strong oxidative ability of $CaMnO_3$/g-C_3N_4 photocatalyst, the composite may be applied to the degradation of other organic pollutants in the future.

5 Conclusions

In this study, a durable $CaMnO_3$/g-C_3N_4 heterostructure has been successfully engineered. This heterostructure exhibited improved performance in the photocatalytic degradation of TC compared to g-C_3N_4 alone, owing to its increased specific surface area, enhanced visible-light absorption, and superior efficiency in separating photogenerated charge carriers. Additionally, $CaMnO_3$/g-C_3N_4 demonstrated exceptional stability, maintaining consistent photocatalytic efficiency even after undergoing 5 cycling tests. Through a combination of free radical trapping experiments and ESR measurements, h^+ and $^{\cdot}O^{2-}$ were identified to be the primary free radicals involved in TC degradation process, with $^{\cdot}$OH playing a secondary role. Based on these findings, a potential reaction mechanism for TC degradation over $CaMnO_3$/g-C_3N_4 photocatalyst is proposed. We believe this research will pave the way for the creation of cost-effective and efficient photocatalysts aimed at removing antibiotics from wastewater.

Data availability

The original contributions presented in this work are included in the article, further inquiries can be directed to the corresponding author.

Author contributions

Bo Zhang: methodology, data curation, writing – original draft preparation. Chaoqi Li: methodology, data curation, writing. Shasha Liu: data curation, validation, writing. Lixuan Zhuang: data curation, formal analysis. Weiqi Zhang: data curation, formal analysis. Limei Huang: data curation, formal analysis. Zhenzhen, Jia: methodology, data curation, formal analysis. Dongdong Chen and Xiang Li conceived the idea, designed the study, analysed the data, and cowrote the paper.

Conflicts of interest

The authors declare no conflict of interest.

Acknowledgements

The research received financial support from the Zhaoqing City Science and Technology Innovation Guidance Project (No. 2023040304001), the Zhaoqing University Natural Science Project (ZD202408), Innovative Team for Ecotoxicology and Remediation of New Pollutants at Zhaoqing University (TD202418), and the Innovative Entrepreneurship Project for Chinese College Students (S202310580066, 202410580016, 202410580017, 202410580018).

References

1 F. Wang, J. Xu, Z. Wang, Y. Lou, C. Pan and Y. Zhu, *Appl. Catal., B*, 2022, **312**, 121438.
2 V. Maroga Mboula, V. Héquet, Y. Gru, R. Colin and Y. Andrès, *J. Hazard. Mater.*, 2012, **209–210**, 355–364.
3 Z. Xu, S. Gong, W. Ji, S. Zhang, Z. Bao, Z. Zhao, Z. Wei, X. Zhong, Z.-T. Hu and J. Wang, *Chem. Eng. J.*, 2022, **446**, 137009.
4 P. P. Singh, G. Pandey, Y. Murti, J. Gairola, S. Mahajan, H. Kandhari, S. Tivari and V. Srivastava, *RSC Adv.*, 2024, **14**, 20492–20515.
5 Y. Liang, W. Xu, J. Fang, Z. Liu, D. Chen, T. Pan, Y. Yu and Z. Fang, *Appl. Catal., B*, 2021, **295**, 120279.
6 K. Wu, D. Chen, S. Lu, J. Fang, X. Zhu, F. Yang, T. Pan and Z. Fang, *J. Hazard. Mater.*, 2020, **382**, 121027.
7 D. Chen, S. Wu, J. Fang, S. Lu, G. Zhou, W. Feng, F. Yang, Y. Chen and Z. Fang, *Sep. Purif. Technol.*, 2018, **193**, 232–241.
8 V. G. Deonikar, K. Koteshwara Reddy, W.-J. Chung and H. Kim, *J. Photochem.*, 2019, **368**, 168–181.
9 D. Chen, J. Liu, Z. Jia, J. Fang, F. Yang, Y. Tang, K. Wu, Z. Liu and Z. Fang, *J. Hazard. Mater.*, 2019, **361**, 294–304.
10 D. Chen, J. Fang, S. Lu, G. Zhou, W. Feng, F. Yang, Y. Chen and Z. Fang, *Appl. Surf. Sci.*, 2017, **426**, 427–436.
11 Y. Narita, K. Nishi, T. Matsuyama and J. Ida, *RSC Adv.*, 2024, **14**, 20898–20907.
12 X. Zeng, S. Shu, Y. Meng, H. Wang and Y. Wang, *Chem. Eng. J.*, 2023, **456**, 141105.
13 T. Jiang, Z. Wang, G. Wei, S. Wu, L. Huang, D. Li, X. Ruan, Y. Liu, C. Jiang and F. Ren, *ACS Energy Lett.*, 2024, **9**, 1915–1922.
14 L. Mao, B. Zhai, J. Shi, X. Kang, B. Lu, Y. Liu, C. Cheng, H. Jin, E. Lichtfouse and L. Guo, *ACS Nano*, 2024, **18**, 13939–13949.
15 H. Wang, L. Yu, J. Peng, J. Zou and J. Jiang, *J. Mater. Sci. Technol.*, 2025, **208**, 111–119.
16 L. Chen, M. A. Maigbay, M. Li and X. Qiu, *Adv. Powder Mater.*, 2024, **3**, 100150.
17 Y. Wang, M. Ding, Z. Li and M. Li, *Surface. Interfac.*, 2024, **44**, 103585.
18 W. He, L. Liu, T. Ma, H. Han, J. Zhu, Y. Liu, Z. Fang, Z. Yang and K. Guo, *Appl. Catal., B*, 2022, **306**, 121107.
19 P. Zhu, M. Hu, M. Duan, L. Xie and M. Zhao, *J. Alloys Compd.*, 2020, **840**, 155714.
20 A. Mehtab and T. Ahmad, *ACS Catal.*, 2024, **14**, 691–702.
21 A. H. Navidpour, J. Safaei, M. A. H. Johir, B.-J. Ni, A. Dashti, X. Li and J. L. Zhou, *Adv. Compos. Hybrid Mater.*, 2024, **7**, 53.
22 G. Chen, W. Ding, W. Dong, H. Wang, S. Zhu, T. Liang, C. Luo and Y. Huang, *Chem. Eng. J.*, 2024, **483**, 149152.
23 T. Ahamad and S. M. Alshehri, *Sep. Purif. Technol.*, 2022, **297**, 121431.
24 G. Mamba, P. J. Mafa, V. Muthuraj, A. Mashayekh-Salehi, S. Royer, T. I. T. Nkambule and S. Rtimi, *Mater. Today Nano*, 2022, **18**, 100184.
25 A.-U.-R. Bacha, I. Nabi, Y. Chen, Z. Li, A. Iqbal, W. Liu, M. N. Afridi, A. Arifeen, W. Jin and L. Yang, *Coord. Chem. Rev.*, 2023, **495**, 215378.
26 M. Irshad, Q. t. Ain, M. Zaman, M. Z. Aslam, N. Kousar, M. Asim, M. Rafique, K. Siraj, A. N. Tabish, M. Usman, M. u. Hassan Farooq, M. A. Assiri and M. Imran, *RSC Adv.*, 2022, **12**, 7009–7039.
27 B. Barrocas, S. Sério, A. Rovisco and M. E. Melo Jorge, *J. Phys. Chem. C*, 2014, **118**, 590–597.
28 M. A. Ferreira, G. T. S. T. da Silva, O. F. Lopes, V. R. Mastelaro, C. Ribeiro, M. J. M. Pires, A. R. Malagutti, W. Avansi and H. A. J. L. Mourão, *Mater. Sci. Semicond. Process.*, 2020, **108**, 104887.
29 C. Liu, M. Chen, Q. Ye, P. Wu, J. Liu, J. Wu, Z. Shang, W. Niu and N. Zhu, *J. Environ. Chem. Eng.*, 2023, **11**, 109845.
30 T. Wang, X. Qian, D. Yue, X. Yan, H. Yamashita and Y. Zhao, *Chem. Eng. J.*, 2020, **398**, 125638.
31 X. Y. Yu, F. S. Li, C. S. Huang, H. Fang and Z. H. Xu, *J. Mater. Res. Technol.*, 2020, **9**, 6595–6601.
32 J. Su, H. Zhao, R. Yang, B. Wang, Y. Xu, X. Lin, Y. Xie and C. Wang, *Ceram. Int.*, 2023, **49**, 32049–32057.
33 B. Bulfin, J. Vieten, D. E. Starr, A. Azarpira, C. Zachäus, M. Hävecker, K. Skorupska, M. Schmücker, M. Roeb and C. Sattler, *J. Mater. Chem. A*, 2017, **5**, 7912–7919.
34 L. Chang, J. Li, Z. Le, P. Nie, Y. Guo, H. Wang, T. Xu and X. Xue, *J. Colloid Interface Sci.*, 2021, **584**, 698–705.
35 J. Macan, F. Brleković, S. Kralj, A. Supina, D. Gracin, A. Šantić and A. Gajović, *Ceram. Int.*, 2020, **46**, 18200–18207.
36 Y. Hu, X. Han, Q. Zhao, J. Du, F. Cheng and J. Chen, *J. Mater. Chem. A*, 2015, **3**, 3320–3324.
37 K. R. Nandan and A. R. Kumar, *J. Mater. Res. Technol.*, 2019, **8**, 2996–3003.
38 S. Biniazi, H. Asgharzadeh, I. Ahadzadeh, Ö. Aydın and M. Farsak, *Dalton Trans.*, 2022, **51**, 18284–18295.

39 M. Madi and M. Tahir, *Mater. Sci. Semicond. Process.*, 2022, **142**, 106517.
40 M. Zhang, C. Lai, B. Li, F. Xu, D. Huang, S. Liu, L. Qin, X. Liu, H. Yi, Y. Fu, L. Li, N. An and L. Chen, *Chem. Eng. J.*, 2021, **422**, 130120.
41 X. Wu, Q. Zhao, F. Guo, G. Xia, X. Tan, H. Lv, Z. Feng, W. Wu, J. Zheng and M. Wu, *Carbon*, 2021, **183**, 628–640.
42 Z.-A. Lan, G. Zhang and X. Wang, *Appl. Catal., B*, 2016, **192**, 116–125.
43 M. Zhou, D. Yoon, Y. Yang, L. Zhang, C. Li, H. Wang, A. Sharma, S. Jiang, D. A. Muller, H. D. Abruña and J. Fang, *ACS Energy Lett.*, 2023, **8**, 3631–3638.
44 R. Cao, H. Yang, S. Zhang and X. Xu, *Appl. Catal., B*, 2019, **258**, 117997.
45 G.-X. Huang, C.-Y. Wang, C.-W. Yang, P.-C. Guo and H.-Q. Yu, *Environ. Sci. Technol.*, 2017, **51**, 12611–12618.
46 C. Chen, Y. Zhou, N. Wang, L. Cheng and H. Ding, *RSC Adv.*, 2015, **5**, 95523–95531.
47 R. Parvari, F. Ghorbani-Shahna, A. Bahrami, S. Azizian, M. J. Assari and M. Farhadian, *J. Photochem.*, 2020, **399**, 112643.
48 F. Al Marzouqi, Y. Kim and R. Selvaraj, *New J. Chem.*, 2019, **43**, 9784–9792.
49 N. Hallemans, D. Howey, A. Battistel, N. F. Saniee, F. Scarpioni, B. Wouters, F. La Mantia, A. Hubin, W. D. Widanage and J. Lataire, *Electrochim. Acta*, 2023, **466**, 142939.
50 Y. Zhang, H. Zhang, J. Yao, Y. Song, W. Li and X. Xuan, *Chem. Eng. J.*, 2024, **483**, 149326.
51 X. Jiang, S. Chen, X. Zhang, L. Qu, H. Qi, B. Wang, B. Xu and Z. Huang, *Adv. Compos. Hybrid Mater.*, 2023, **6**, 47.
52 Q. Chen, H. Zhou, J. Wang, J. Bi and F. Dong, *Appl. Catal., B*, 2022, **307**, 121182.
53 H. Leelavathi, R. Muralidharan, N. Abirami and R. Arulmozhi, *New J. Chem.*, 2023, **47**, 7774–7789.
54 Z. Tang, C. Hu, R. Zhang, J. Yu, L. Cai, Z. Yang, X. Wang, S. Wu and D. Liu, *RSC Adv.*, 2024, **14**, 15302–15318.